Chinese Chemical Letters 35 (2024) 109001

Contents lists available at ScienceDirect

Chinese Chemical Letters

journal homepage: www.elsevier.com/locate/cclet

Oxygen self-doping pyrolyzed polyacrylic acid as sulfur host with physical/chemical adsorption dual function for lithium-sulfur batteries

Yan Wang[a,c,1], Huixin Chen[b,c,1], Fuda Yu[a], Shanyue Wei[a,c], Jinhui Song[c], Qianfeng He[c], Yiming Xie[a,*], Miaoliang Huang[a,*], Canzhong Lu[b,c,*]

[a] Engineering Research Center of Environment-Friendly Functional Materials, Ministry of Education, Institute of Materials Physical Chemistry, Huaqiao University, Xiamen 361021, China
[b] CAS Key Laboratory of Design and Assembly of Functional Nanostructures, and Fujian Provincial Key Laboratory of Nanomaterials, Fujian Institute of Research on the Structure of Matter, Chinese Academy of Sciences, Fuzhou 350002, China
[c] Xiamen Key Laboratory of Rare Earth Photoelectric Functional Materials, Xiamen Institute of Rare Earth Materials, Haixi Institutes, Chinese Academy of Sciences, Xiamen 361021, China

ARTICLE INFO

Article history:
Received 27 June 2023
Revised 9 August 2023
Accepted 28 August 2023
Available online 1 September 2023

Keywords:
Polyacrylic acid
Oxygen self-doping
Green synthetic
Pore mesh polymer cathodes
Lithium-sulfur batteries

ABSTRACT

Lithium-sulfur (Li-S) batteries with high theoretical capacity and energy density need to solve problems such as the high decomposition energy barrier of Li_2S and large volume change of sulfur in the charging process caused by the shuttle effect before practical application. Herein, a green synthesis method is used to prepare polyacrylic acid (PAA) superabsorbent material, and then the pyrolyzed PAA (P/PAA) material is obtained as the positive electrode of Li-S battery. Density functional calculation reveals that the oxygen self-doping pyrolyzed polyacrylic acid (P/PAA) delivered stronger binding energy toward Li_2S species in carbonyl C=O than that of graphite powder (GP) which are −1.58 eV and −1.02 eV, respectively. Coupled with the distribution of relaxation time analysis and the *in-situ* electrochemical impedance approach, it is further demonstrated that the designed P/PAA as sulfur host plays a physical/chemical adsorption dual function in maintaining the stability and rate performance of batteries. With an initial discharge capacity of 1258 mAh/g at 0.1 C and a minimal capacity decline of 0.05% per cycle even after 800 cycles at 0.5 C, the produced cathode demonstrated outstanding electrochemical performance. The average Coulombic efficiency is nearly 100%. The P/PAA electrodes may typically retain 96% of their capacity while declining on average only 0.033% per cycle after 130 cycles at 3 C. This effort provides a new method for the future development of heteroatomic self-doping superabsorbent with promising adsorption properties for polysulfides as cathode materials of Li-S batteries.

Because of their impressive theoretical capacities (1675 mAh/g) and energy densities (2600 Wh/kg), which are closely tenfold greater than those of Li-ion batteries according to conventional cathode materials such as transition metal oxides, lithium-sulfur (Li-S) batteries are attracting significant attention [1–4]. In addition, sulfur is harmless and inexpensively available, which favors large-scale uses. Despite these advantages, commercializing Li-S batteries is still incredibly difficult [5–8]. In specific, sulfur's final discharge product (Li_2S), which is neither electronically nor ionically conductive, and sulfur has an electrical conductivity of only about 5×10^{-30} S/cm at room temperature, and the significant volumetric variation of sulfur (80%) during lithiation causes the loss of active material [9,10]. Moreover, during the intricate multielectron electrochemistry of Li-S batteries, the soluble lithium polysulfides (LiPSs) in the electrolyte shuttle between a cathode and a Li anode, resulting in serious capacity reduction and poor Coulombic efficiency [11–14]. In order to resolve these issues and enhance the performance of Li-S batteries, several types of porous materials, such as porous carbon [15,16], carbon nanotubes [17,18], porous organic polymers [19,20], and metal-organic frameworks [21,22], have been developed to prepare as hosts to absorb and anchor LiPSs.

Although the discharge capacity of Li-S batteries has been significantly increased by C/S composite cathodes, the openness of the pore structure and the weak van der Waals force between nonpolar carbon materials and LiPSs could not prevent the inevitable dissolution of active substance sulfur in the electrolyte, leading to

* Corresponding authors.
E-mail addresses: ymxie@hqu.edu.cn (Y. Xie), huangml@hqu.edu.cn (M. Huang), czlu@fjirsm.ac.cn (C. Lu).
[1] These authors contributed equally to this work.

https://doi.org/10.1016/j.cclet.2023.109001
1001-8417/

a quick decline in capacity during prolonged cycles. In this context, heteroatoms-doped carbonaceous materials like the extremely electronegative N, O, P, S, *etc*. [23–27], and polar metal-based materials like metal phosphides, metal oxides, and metal-organic frameworks [28–31] are particularly appealing hosts due to their strong interaction with LiPSs that effectively mitigates the shuttling effect [32,33].

In this work, we fabricated a cathode material with porous mesh for high-performance Li-S batteries using green synthetic polyacrylic acid superabsorbent material. Specifically, the pyrolyzed polyacrylic acid (P/PAA) synthesized by the green method could provide more attachment sites for simple sulfur and space for its volume expansion owing to its porous network structure. Meanwhile, the existence of polar carbonyl groups could form strong adsorption with polysulfide, giving LiPSs a strong link to chemically anchor active ingredients [34–37], and slowing down the shuttle effect. In order to better make clear the underlying mechanics, DFT calculations were put into effect. The findings showed that the existence of a similar Li-O bond effectively anchored LiPSs on P/PAA. The P/PAA played a dual physical/chemical adsorption mechanism on polysulfide by taking advantage of the cooperative impact of the O self-doping element and its porous network structure. Consequently, the S@P/PAA exhibited a minimal capacity decline of 0.05% per turn even after 800 cycles at 0.5 C and the average attenuation per turn was just 0.033% after 130 cycles at 3 C. This study is believed to inspire new ideas for the practical utilization of self-doping superabsorbent materials with exceptional adsorption capabilities for LiPSs as cathode materials in Li-S batteries. Next is the preparation process of P/PAA material, S@P/PAA and S@GP batteries.

Synthesis of the pyrolyzed polyacrylic acid (P/PAA): Typically, pour 50 mL (6.5 mol/L) sodium hydroxide solution into a beaker containing 30 mL acrylic monomer for neutralization. When the reaction temperature dropped to 80 °C, 0.0147 g *N*,*N*'-methylene diacrylamide was quickly added as a crosslinking agent, and 0.1176 g potassium persulfate initiator was added for cross-linking copolymerization reaction. The reaction temperature was further raised to complete the reaction. At the end of the reaction, the bulk body with bubbles in the middle was obtained. With the use of scissors, the product was divided into small pieces, then dried for 8 h at 80 °C in a vacuum oven.

The dried polyacrylic acid (PAA) composite was pyrolyzed in a tube furnace at 500 °C for 1.5 h and at 800 °C for 2 h, both times with a heating rate of 5 °C/min under Ar atmosphere. After cooling to room temperature, the P/PAA material was obtained.

Synthesis of the S@P/PAA and S@GP composites: The S@pyrolyzed Polyacrylic acid (S@P/PAA) and S@graphite powder (S@GP) composites were prepared by using the traditional melt-diffusion process. The P/PAA and GP samples were combined with S powder in a mass ratio of 2:3 and kept in a Celine bottle before being annealed at 155 °C for 12 h to make sulfur completely diffuse into the as-fabricated sample.

Scanning electron microscopy (FESEM, HITACHI SU1510) and transmission electron microscopy (TEM) were used to observe the morphology and microstructure of the materials, and the element mapping images were texted by FEI Talos F200X G2 at an accelerating voltage of 200 kV. The Brunauer-Emmett-Teller (BET) and an N_2-adsorption analyzer (Quantachrome Autosorb iQ2) technique were employed in the surface area investigation. X-ray diffraction (XRD) patterns were obtained utilizing a Miniflex 600 diffractometer over the 2θ range 5º-80º, with Cu Kα radiation ($\lambda = 1.54056$ Å). Using a Thermo Scientific K-Alpha with Al-Kα X-ray source ($h\nu = 1486.7$ eV), the X-ray photoelectron spectroscopy (XPS) data were obtained, and the charge corrections value was calculated using the C 1s value set at 284.8 eV. A Renishaw inVi laser confocal microscopic Raman spectrometer with a 522 nm laser excitation source was used to get the Raman spectra. Ultraviolet-visible spectroscopy (UV–vis spectroscopy) was obtained using the Agilent Cary 5000. Thermo-Gravimetric Analysis (Mettler-Toledo TGA/DSC 1) was applied to analyze the weight ratio of sulfur in the composites between 35 and 500 °C at a heating rate of 5 °C/min.

Li-S cells assembly and electrochemical characterizations: The active substance, Ketjenblack and polyvinylidene fluoride (PVDF) binder at a mass ratio of 7:2:1 combined with *N*-methyl-2-pyrrolidone (NMP) as a dispersant to make the cathode slurry, then the slurry was uniformly cast on the aluminum foil and dried at 60 °C for 12 h, and the acquired piece was sliced into a film disk of 12 mm in diameter. The areal mass loading of sulfur was approximately 1.27 mg/cm^2. The CR2025 coin cells were assembled with Li metal as an anode, and 1 mol/L LITFSI + 1 wt% lithium nitrate ($LiNO_3$) dissolved in the mixed solvent of dimethoxyethane (DME) and 1,2-dioxolane (DOL) (1:1, v:v) as an electrolyte, and a microporous polypropylene film (Celgard 2500) was employed as a separator. For the batteries, the electrolyte in the regular sulfur cathodes is about 15 μL/mg. In addition, the coin cells were gathered in a glove box with low oxygen and water content filled with argon.

All batteries were examined with a battery testing system (CT4008T) at a voltage of 1.7–2.8 V (*vs.* Li/Li$^+$) after aging for 4 h at 30 °C. Additionally, at 0.5 and 3 C (1 C = 1675 mAh/g) at 30 °C, the performance of galvanostatic charge-discharge cycling was evaluated. The cyclic voltammetry (CV) and the electrochemical impedance spectroscopy (EIS) were implemented on an electrochemical workstation (CHI760E). With a scan rate of 0.1 mV/s and a voltage range of 1.7 V to 2.8 V, the CV measurements were carried out at room temperature. The 5 mV amplitude and a frequency range of 0.01 Hz to 100 kHz were used for the EIS investigation.

Lithium polysulfides (LiPS) adsorption study: The sublimated sulfur and Li_2S were dissolved in dimethyl ether solution with a molar ratio of 5:1, and stirred at 60 °C until the liquid turned yellow (0.4 mol/L) to obtain Li_2S_6 solution. Then 1 mL 0.4 mol/L polylithium sulfide solution was mixed with 9.0 mL dimethyl ether solution to obtain 10 mL diluted Li_2S_6/DME test solution. For the next 20 min, 60 mg of PAA was put into 10 mL of Li_2S_6/DME solutions next to vigorous stirring, then leave to rest. All of the experiments were carried out in an argon-filled glove box. Finally, the UV-visible absorbance of the supernatant was detected.

Density functional theory calculation: We first used ChemDraw software to draw the basic models of the minimum repetition units of the structural PAA, Li_2S and LiS^-, and then used Chem 3D software for preliminary optimization of the structures. After that, we combined the optimized PAA minimum repetition unit with Li_2S and LiS^- to obtain corresponding structures respectively, and continued to use Chem 3D for reasonable optimization. Density functional theory (DFT) was used to optimize the minimum repetition units, Li_2S, LiS^- and the combined structure of the optimized PAA to obtain the minimum structural energy. Gaussian 16 software and M06–2X (D3) functional were used to optimize the calculation under the condition of 6–311+G**. The three parts are calculated separately, and the energy for *E*(substart), *E*(Li_2S/LiS^-) and *E*(substart + Li_2S/LiS^-), Then according to the formula $E_b = E$(substart + Li_2S/LiS^-) - *E*(substart) - *E*(Li_2S/LiS^-) to obtain corresponding binding energy. The following is the characterization analysis of P/PAA and GP materials, S@P/PAA and S@GP batteries.

The PAA was fabricated using a polymer green synthesis method as shown in Scheme 1 [38]. In short, acrylic monomer, sodium hydroxide, *N*,*N*'-methylene bisacrylamide, and potassium thiosulfate were well mixed, using the heat of polymerization to facilitate the reaction. In order to explore the optimal pyrolysis temperature, the TG-MS of 35–800 °C was performed on the dried

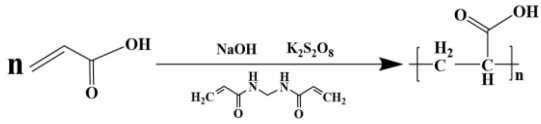

Scheme 1. Synthesis process of polyacrylic acid superabsorbent.

PAA raw material. The curve is shown in Fig. S1 (Supporting information). The data shows that the material tends to be stable at 700–800 °C, so the P/PAA material was finally prepared by carbonization at 800 °C. The results of elemental analysis showed that the oxygen content in P/PAA was 11.92%. After heat treatment and acid treatment, a porous network P/PAA was obtained. SEM and TEM were employed to examine the morphology and microstructure of P/PAA carbon material. Compared with the multilayer poreless structure of GP (Graphite powder, Figs. S2a-c in Supporting information), the obtained P/PAA was composed of a network of continuously connected porous structures in Figs. 1a and b. The surface morphology of S@P/PAA composite obtained by ball milling method was shown in Figs. 1c and d. Meanwhile, the nitrogen adsorption-desorption experiment also clearly confirmed the porous network structural property of P/PAA in Figs. 2a and b. The curves of GP and P/PAA samples were similar to typical type IV isotherms [24], and obvious hysteresis loops can be observed in both of them, which indicated that the material had more mesoporous structures. The specific surface area of GP was just 1.121 m^2/g, while P/PAA demonstrated a specific surface area of 36.167 m^2/g with the pore size was 10.6 nm on average. This structural characteristic may have helped by offering a large number of immobilized LiPSs adsorption sites [39,40]. The TEM images in Figs. 1i and j still illustrated the porous network of P/PAA. Energy dispersive spectroscopy (EDS) mapping in Figs. 1e-h also revealed the presence of carbon (blue), oxygen (green), and sulfur (yellow) in the S@P/PAA, showing the existence of more numerous polar groups and the development of a homogeneous composite with S.

Powder XRD analysis was used to investigate the polymer nature in order to acquire a greater knowledge of the phase composition of P/PAA materials. In Fig. 2c, carbonized PAA polymer displayed two wide distinctive peaks at around 22° and 43°, which were explained as the characteristic peaks of the C (002) and (100) facets [41]. Furthermore, Raman spectra were also utilized to assess the graphitization degree and structuration defect of polymer carbon material [42,43]. Fig. 2d illustrated that the I_D/I_G ratio was 0.96, indicating the formation of defects in the graphitic carbon nanosheets which is induced by O doping [44]. The conductivity of carbon materials was significantly influenced by their degree of graphitization. If carbon materials were employed as positive electrode materials for batteries, good conductivity could significantly improve the electron transfer efficiency in the charge-discharge process, thus enhancing the electrochemical performance of the battery.

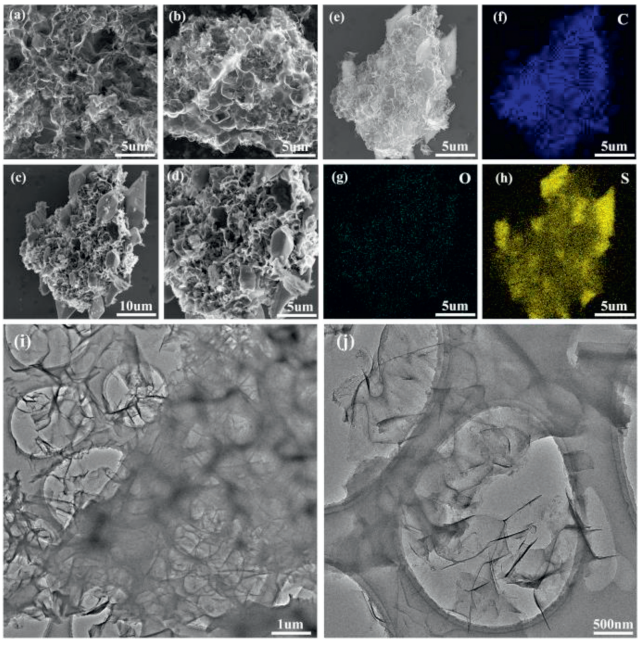

Fig. 1. (a, b) SEM images of P/PAA. (c, d) SEM images of S@P/PAA. (e-h) SEM image and the C, O, S elementals mapping images of S@P/PAA. (i, j) TEM images of P/PAA.

To explore whether elemental sulfur was sufficiently mixed with the PAA carbon material, Fig. 2e revealed the XRD analysis of the fabricated composite cathode materials. Corresponding to the S (PDF#99–0066), it was found that the position of the characteristic peak was the same as that of sulfur, and there was no diffraction peak of the carbon graphitized crystal plane. The finding revealed that sulfur could be well distributed on the surface and pore structures of PAA carbon materials. The content of active substances could be examined by TG-MS in Fig. 2f. The analysis curves revealed that the content of sulfur of both P/PAA and GP was about 60 wt%, indicating that there was almost no loss of active substances in the composite of carbon material prepared by the melting diffusion method.

The surface compositions of the PAA carbon materials were examined by X-ray photoelectron spectroscopy (XPS). Prominent signals of C 1s (~284 eV) and O 1s (~532 eV) can be identified from the XPS survey spectrum as shown in Fig. 3a. Three fitted peaks representing C–C (284.8 eV), C-O (285.8 eV), and C=O (288.9 eV) were shown in the high-resolution C 1s spectra in Fig. 3b [40]. The spectrum of O 1s in Fig. 3c can be deconvoluted into two main peaks at 533.4 eV and 531.7 eV representing C-O and C=O [45]. Additionally, after cycling, the S@P/PAA electrode cell was disassembled, and the sulfur conversion was texted using XPS. The representative doublets for the S_8 molecules can be seen at 162.4 and 163.6 eV in the S 2p spectra in Fig. 3d [46]. The peaks at 167.4 and 169.1 eV, respectively, were attributed to thiosulfate, which was produced owing to polysulfide oxidation on the P/PAA surface [47]. The other two peaks located at about 169.7 and 170.6 eV were considered to be the sulfate reactions originating from the over-oxidation of Li_2S_n by LiTFSI [48,49]. Overall, in the absence of dead sulfides, the S@P/PAA cathode demonstrated remarkable reversibility in transforming the insoluble Li_2S back to long-chain LiPSs. These findings indicated the existence of abundant oxygen groups in the material, and that these abundant polar sites could supply efficient anchoring sites for the polysulfides produced in the charge-discharge process of Li-S batteries, and also greatly improved the electron transport efficiency of the material. Therefore, to confirm the high adsorption of polysulfides in the P/PAA host, visualized polysulfide adsorption experiments were conducted in Fig. 3e. The P/PAA exhibited a decrease in the absorbance strength of the Li_2S_6 solution in the wavelength range of about 270 nm, corresponding to the curve of the S_6^{2-} species [50]. The inserted digital image of Li_2S_6 solution filled with P/PAA turned lightener after 48 h, confirming the proper adsorption capability of P/PAA toward S_6^{2-} species. The unique polysulfide adsorption capability of P/PAA should be attributed to the polar oxygen atoms in its carbonyl group and the unique adsorption site between P/PAA and the polysulfide. Furthermore, the strong interaction between LiPSs and the carbonyl group as well as the naturally porous structure contributed to the superior performance, which strongly suppressed the shuttle effect during charge-discharge.

The *in-situ* EIS was carried out in Fig. 3f and Fig. S3 (Supporting information) to reveal the kinetics of S@P/PAA during polysul-

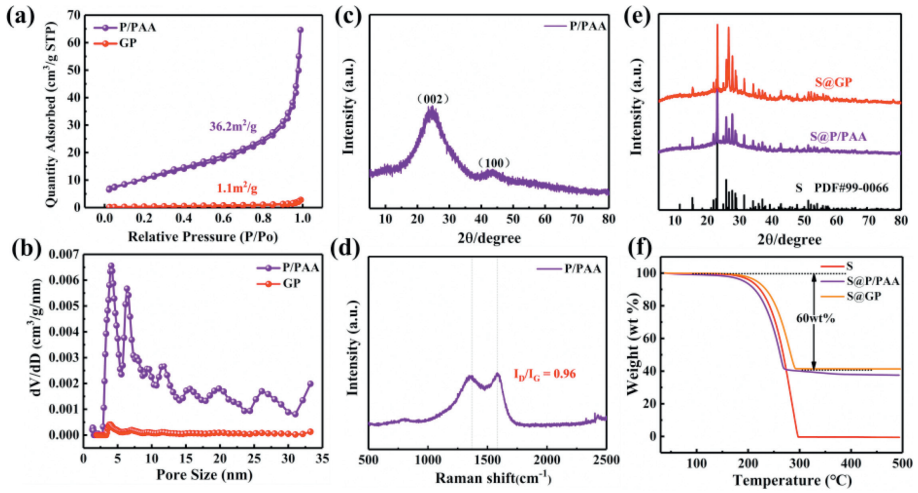

Fig. 2. (a) N_2 adsorption/desorption isotherms and (b) pore size distribution curves for P/PAA and GP. (c) XRD patterns and (d) Raman spectra for P/PAA. (e) XRD patterns for S@P/PAA and S@GP. (f) TG results of S@P/PAA and S@GP under argon atmosphere from 35 °C to 500 °C.

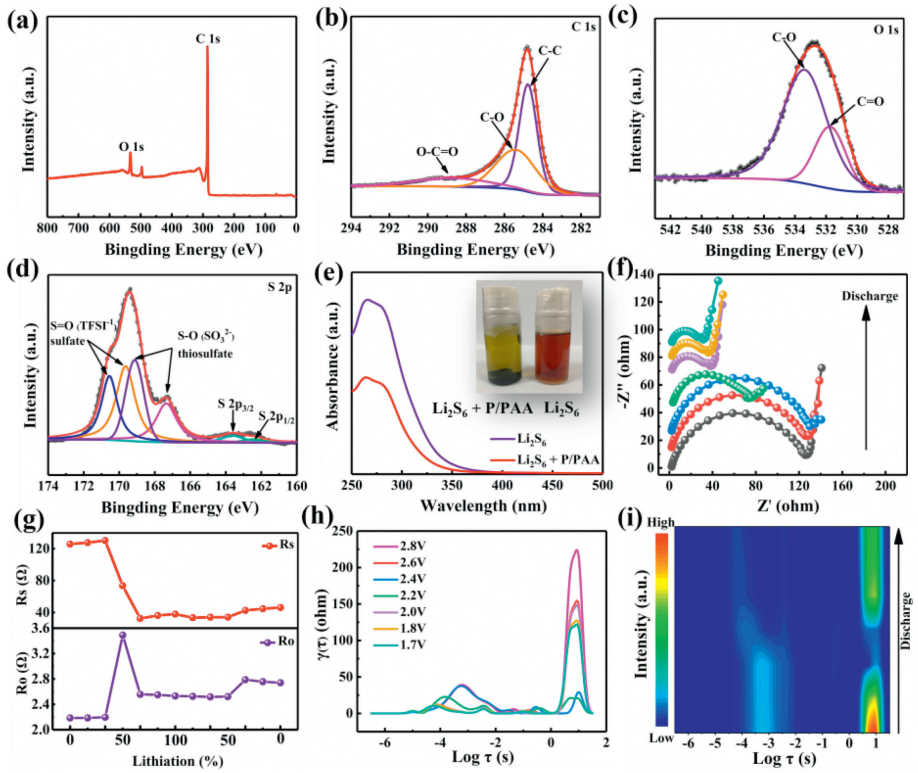

Fig. 3. (a) The total XPS spectra, and the XPS spectras of (b) C 1s, and (c) O 1s of P/PAA. (d) The XPS spectra of the S@P/PAA electrode after cycling. (e) UV absorption spectra of Li_2S_6 solution with P/PAA, the inset is the digital images. (f) *In-situ* EIS characterizations of S@P/PAA during discharge. (g) Variations of Ro and Rs calculated from the EIS curves. (h) DRT calculated from EIS measurements at different discharge states. (i) 2D intensity color map of the discharge-dependent DRT curves.

fide redox processes. Typically, the sections of the EIS curves were represented by the Warburg impedance (W_o), interfacial resistance (R_s), and the electrolyte's internal resistance (R_o) [51,52]. According to Fig. 3g, the Ro value was found to be low during the initial discharge stages and slightly increased with the increase of discharge depth, which may be related to the electrolyte's viscosity changing as a result of the little LiPSs dissolving [53,54]. Due to the oxidation of the LiPSs to insolvable Li_2S, the Ro dropped as the depth of the discharge rose. Concurrently, the value of Rs rose owing to the production of Li_2S. and all the variations were reversed throughout the charging procedure, indicating the quick kinetics of sulfur conversion in S@P/PAA. To further confirm that the Li-S battery with S@P/PAA was stable and reversible, the EIS spectra were studied by a semiquantitative distribution utilizing relaxation time (DRT) in Fig. 3h and Fig. S4 (Supporting information). A more pronounced alteration in the intensity color map of the discharge-dependent DRT curves was displayed in Fig. 3i. In general, the kinetics of the enhanced sulfur cathode was faster, which reflected that the shuttle of LiPSs could be slowed down owing to strong adsorption ability and anchoring properties.

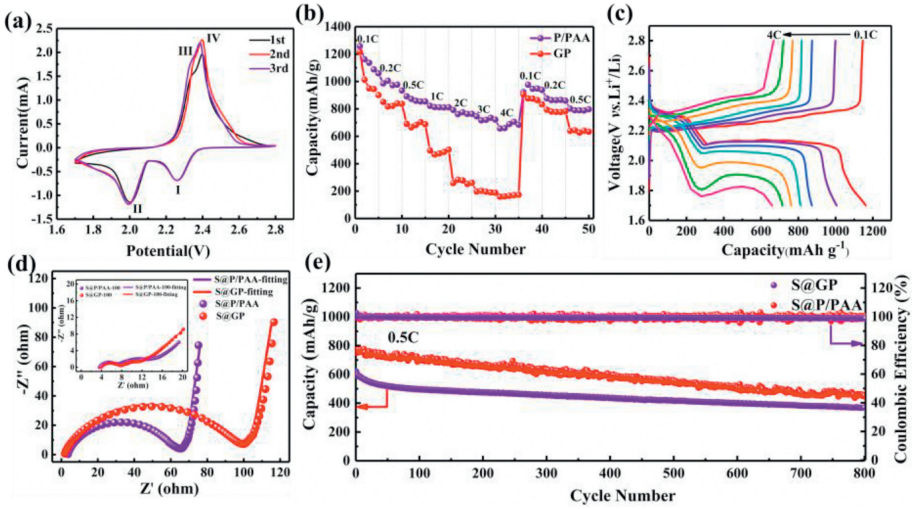

Fig. 4. (a) Cyclic voltammetry curves of S@P/PAA cell. (b) Rate capability of S@P/PAA and S@GP electrodes. (c) Charge-discharge curves of the second turn of the S@P/PAA electrode at different current rates. (d) Electrochemical Impedance Spectroscopy recorded of S@P/PAA and S@GP electrodes. (e) Cycling performances of S@P/PAA and S@GP electrodes at 0.5 C.

To further reveal the role of the carbonyl groups, density functional theory (DFT) calculations were employed to simulatethe binding energies ($E_{binding}$) between P/PAA and Li_2S/LiS^- (see Supporting information for details). The optimized geometries of Li_2S/LiS^- and its adsorption on P/PAA and GP carbon materials with the lowest binding energy were displayed in Fig. S5 (Supporting information). The calculated binding energies of an oxygen atom with Li_2S and LiS^- in C–O were 14.21 eV and 15.58 eV, and the binding energies of an oxygen atom with Li_2S and LiS^- in carbonyl C=O were −1.58 eV and −1.52 eV, respectively. It can be seen that the oxygen atoms in the carbonyl group were more likely to combine with the polysulfide to form ligands similar to the Li-O bonds in P/PAA carbon materials [55,56]. Moreover, the binding energy of Li_2S with P/PAA and GP were calculated. The P/PAA delivered stronger binding energy toward Li_2S species than this of GP carbon material which was −1.02 eV. This interaction pattern was consistent with previous reports on the interaction between polysulfide and organic molecules [49,57]. The stronger binding energy exhibited a strong bonding, which can improve LiPSs anchoring and reduce the shuttle effect during the charge-discharge process of Li-S batteries.

The electrochemical performance of S@P/PAA cathode in Li-S batteries were tested at a voltage range of 1.7–2.8 V with a scan rate of 0.1 mV/s. As displayed in Fig. 4a, two remarkable cathodic peaks I (2.26 V) and peaks II (1.99 V) in the CV curves, which can be attributed to the conversion of S_8 to high soluble polysulfide and further reduction to solid Li_2S_2/Li_2S, respectively [58,59]. In addition, the obvious anodic peak III (2.34 V) and IV (2.39 V) matched the conversion process from solid Li_2S/Li_2S_2 to soluble polysulfides, and lastly to S_8, respectively [60]. The cyclic voltammetry (CV) curves of S@P/PAA in three cycles demonstrated that the oxidation and reduction peak positions, peak areas, and cycle paths remain almost unchanged. This was attributed to the accelerated redox kinetics of polysulfides on P/PAA, which effectively reduced electrochemical polarization [59]. We selected S@P/PAA and S@GP as the cathode materials for Li-S batteries, and drew the charge-discharge curve of the batteries, as displayed in Fig. 4c and Fig. S6 (Supporting information). Combined with Fig. 4a, it can be seen that the charging and discharging platforms correspond to the redox peaks respectively. The platform with a higher voltage of 2.2–2.3 V represented the solid-liquid transformation process of S_8 molecules into long-chain polysulfide. Because of the high solubility of long-chain polysulfide, the transformation rate was faster at this stage. The second voltage platform at 1.9–2.1 V represented the conversion process of high-order polysulfide dissolved in the electrolyte to low-order polysulfide and insoluble Li_2S_2 and Li_2S [61]. The reaction rate of this process was relatively slow, providing most of the specific discharge capacity, and the degree of electrode polarization was large. The charging platform represented the opposite process of discharge, both of which correspond to the CV curve. In addition, we can see from Fig. 4c that the discharge voltage platform of the material decreases with the rise of the current density, indicating that with the increase of the discharge current, the polarization phenomenon of different degrees appears inside the battery assembled by these composite positive materials, thus increasing the electrochemical reaction resistance of the Li-S batteries during the charge-discharge process. This can also be known from the fact that CV curves do not incompletely coincide in different cycles.

Additionally, as shown in Fig. 4b, the rate capabilities of S@P/PAA and S@GP batteries at various rates from 0.1 C to 4 C (1 C = 1675 mAh/g) were investigated. The initial discharge capacity of the S@GP electrode was 1216 mAh/g at 0.1 C compared to the S@P/PAA electrode (1258 mAh/g), which revealed that P/PAA electrodes used sulfur more efficiently. The cell using the S@P/PAA electrode achieved higher discharge capacities of 985, 892, 823, 792, 746, and 657 mAh/g at the rates of 0.2, 0.5, 1, 2, 3, and 4 C, respectively, which exceeded S@GP with the discharge capacities of 851, 691, 497, 258, 197 and 159 mAh/g, respectively. For S@P/PAA cell, high discharge capacities of 976.6, 876.7, and 801.5 mAh/g could be attained when the rate recovered to 0.1, 0.2, and 0.5 C, respectively, revealing the outstanding electrochemical reversibility and rapid conversion efficiency of polysulfides. In addition, the long-term cycling stabilities of the S@P/PAA with the sulfur mass loading of 1.2 mg/cm^2. A high initial discharge capacity of 759.1 mAh/g was achieved by the S@P/PAA cathode, according to Fig. 4e, and this capacity maintained at 452.4 mAh/g after 800 cycles with the average capacity decay rate of 0.05% per cycle, while with the average capacity decay rate of the S@P/PAA battery was also 0.05% per cycle, and the Coulombic efficiency (CE) were both close to 100%. Furthermore, the S@P/PAA cathode with a sulfur loading of 1.0 mg/cm^2 can generally maintain a capacity retention of 96% at 3 C and the average attenuation per cycle was just 0.033% after 130 cycles in Fig. S7 (Supporting information). The corresponding charge-discharge curves of the S@P/PAA and S@GP cathodes at different rates were shown in Fig. 4c and Fig. S6 (Sup-

porting information). The charge-discharge curves of the S@P/PAA cathode still preserve two discharge plateaus despite the fact that the polarization was raised after extensive cycling, showing better reversibility than the S@GP cathode.

The EIS data of the S@P/PAA and S@GP cathodes initially and after 100th cycles at 0.5 C were displayed in Fig. 4d and the corresponding equivalent circuit was displayed in Fig. S8 (Supporting information) [62]. In the impedance spectrum, the minimum value on the real axis showed the contribution of the electrolyte resistance (R_s) to the impedance. The high-frequency semicircle represented the contact resistance (semicircle diameter, R_{sei}); The intermediate frequency semicircle represented the charge transfer resistance (R_{ct}) [63]. The EIS spectra demonstrated a smaller initial impedance of PAA (59 Ω, $R_{sei}+R_{ct}$) compared to GP (95 Ω, $R_{sei}+R_{ct}$), which was attributed to the electrolyte's better wettability promoting the transport of ions. Another newly depressed semicircle associated with solid Li_2S_2/Li_2S appearing on the electrode and electrolyte interface could be seen when comparing the initial EIS data of the S@P/PAA and S@GP cathodes with those after 100 cycles at 0.5 C. After fitting the equivalent circuit, the Nyquist plots of the two cathodes include two semicircles in the high-frequency region and a diagonal line in the low-frequency region, respectively, representing the impedance, charge transfer resistance and semiinfinite Warburg diffusion process of the passivated film [64]. The impedance of the passivation film, and charge transfer resistance of the S@P/PAA cathode were 2.8 Ω (R_{sei}) and 6.3 Ω (R_{ct}) respectively, which were close to those of the S@GP cathode (3.5 Ω, R_{sei} and 3.3 Ω, R_{ct}), showing that LiPSs were effectively suppressed and that charge transport and electrolyte infiltration were improved. The EIS resistance was reduced due to the fact that the conductive layers effectively alleviated the formation of solid Li_2S_2/Li_2S films and improved the mass transport after 100 cycles [65]. The resistance values of PAA, GP, PAA-100, GP-100 fitted from the equivalent circuits of EIS was displayed in Table S1 (Supporting information).

In conclusion, O self-doping elements and the pore mesh structures of the S@P/PAA cathode are designed to promote chemical anchoring and physical adsorption of polysulfide for advanced Li-S batteries. The S@P/PAA cathode plays a dual physical/chemical adsorption mechanism on polysulfide due to its structural characteristics. The findings demonstrate that a high degree of graphitization, a porous structure with enough voids, and a doping abundance of polar elements can greatly enhance the electrochemical performance of Li-S batteries. Moreover, the binding energies of an oxygen atom with Li_2S and LiS^- in carbonyl C=O are −1.58 eV and −1.52 eV respectively according to the DFT calculation. The P/PAA delivers stronger binding energy toward Li_2S species than this of GP carbon material which is −1.02 eV. Based on the above data, it is evident that the adsorption of oxygen atoms to carbonyl C=O results in polysulfide ligands that resemble Li-O bonds in P/PAA carbon materials. Combined with the *in-situ* EIS method and DRT analysis, it is further demonstrated that oxygen self-doping P/PAA displays physical and chemical adsorption to enhance the stability and reversibility of batteries. The S@P/PAA cathode demonstrates an impressive initial capacity of 1258 mAh/g at 0.1 C and a minimal capacity decline of 0.046% per cycle even after 1000 cycles at 0.5 C. Furthermore, because of the synergistic effect of the oxygen-rich self-doping and porous structures, the shuttle effect has been successfully suppressed through chemical bonding and physical adsorption of polysulfides. We believe that the ingenious design will inspire new ideas for the optimal adsorption-conversion cathode design for the practical utilization of Li-S batteries in the future. This work is eco-friendly and has significant promise for polar porous carbon material applications in energy storage, medicine, and other relevant sectors.

Declaration of competing interest

The authors declare that they have no known competing financial interests or personal relationships that could have appeared to influence the work reported in this paper.

Acknowledgments

The authors thank the financial support of the National Natural Science Foundation of China (Nos. 22271106, 21501175 and 2227518), the Natural Science Foundation of Fujian Province (No. 2022Y0071), the Leading Project Foundation of Science Department of Fujian Province (No. 2023H0045). The authors thank Instrumental Analysis Center of Huaqiao University for Transmission electron microscopy (TEM) and Raman spectrum tests. The authors thank Mr. JunYu Zhang at Instrumental Analysis Center of Huaqiao University for his assistance with TEM analysis and would like to thank Shiyanjia Lab for the X-ray photoelectron spectroscopy test (www.shiyanjia.com).

Supplementary materials

Supplementary material associated with this article can be found, in the online version, at doi:10.1016/j.cclet.2023.109001.

References

[1] L. Shen, Y.-W. Song, J. Wang, et al., Small Struct. 4 (2022) 2200205.
[2] J. He, A. Bhargav, A. Manthiram, Adv. Mater. 32 (2020) 2004741.
[3] L. Ni, S. Duan, H. Zhang, et al., Carbon 182 (2021) 335–347.
[4] Q. Liu, Y. Wu, D. Li, et al., Adv. Mater. 35 (2023) 2209233.
[5] Y.-W. Song, L. Shen, N. Yao, et al., Chem 8 (2022) 3031–3050.
[6] W. Tian, H. Zhang, X. Duan, et al., Adv. Funct. Mater. 30 (2020) 1909265.
[7] B. Amruth, C.H. Chang, Y.Z. Fu, M. Arumugam, ACS Appl. Mater. Interfaces 11 (2019) 6136–6142.
[8] Y. Yan, X. Liu, Chin. Chem. Lett. 34 (2023) 108032.
[9] M. Rana, B. Luo, M.R. Kaiser, I. Gentle, R. Knibbe, J. Energy Chem. 42 (2020) 195–209.
[10] P. Liu, Y. Wang, J. Liu, J. Energy Chem. 34 (2019) 171–185.
[11] Z.X. Chen, L.P. Hou, C.X. Bi, et al., Energy Storage Mater. 53 (2022) 315–321.
[12] M. Yan, Z.Y. Wang, G.W. Yu, et al., Small 18 (2022) 2201822.
[13] L. Zhou, D.L. Danilov, R.A. Eichel, P.H.L. Notten, Adv. Energy Mater. 11 (2021) 2001304.
[14] F. Qi, Z. Sun, X. Fan, et al., Adv. Energy Mater. 11 (2021) 2100387.
[15] S. Rehman, X. Gu, K. Khan, et al., Adv. Energy Mater. 6 (2016) 1502518.
[16] X. Ji, K.T. Lee, L.F. Nazar, Nat. Mater. 8 (2009) 500–506.
[17] Y. Zhao, W. Wu, J. Li, Z. Xu, L. Guan, Adv. Mater. 26 (2014) 5113–5118.
[18] C. Tang, Q. Zhang, M.Q. Zhao, et al., Adv. Mater. 26 (2014) 6100–6105.
[19] Z.B. Cheng, H. Pan, H. Zhong, et al., Adv. Funct. Mater. 28 (2018) 1707597.
[20] Z. Wang, S. Wang, Electrochim. Acta 306 (2019) 229–237.
[21] X. Xiao, L. Zou, H. Pang, Q. Xu, Chem. Soc. Rev. 49 (2020) 301–331.
[22] S.H. Kim, J.S. Yeon, R. Kim, K.M. Choi, H.S. Park, J. Mater. Chem. A 6 (2018) 24971–24978.
[23] S. Yu, Y. Zhang, S. Yang, et al., Chin. Chem. Lett. 34 (2023) 107911.
[24] Y. Zhao, Z. Gu, W. Weng, et al., Chin. Chem. Lett. 34 (2023) 107232.
[25] O. Ogoke, S. Hwang, B. Hultman, et al., J. Mater. Chem. A. 7 (2019) 13389–13399.
[26] H. Li, B. Cai, Y. Song, W. Cai, G. Li, Chin. Chem. Lett. 34 (2023) 107811.
[27] S. Jiang, S. Huang, M. Yao, et al., Chin. Chem. Lett. 31 (2020) 2347–2352.
[28] X. Liu, J.Q. Huang, Q. Zhang, L. Mai, Adv. Mater. 29 (2017) 1601759.
[29] C.L. Wang, L.S. Sun, K. Li, et al., ACS Appl. Mater. Interfaces 12 (2020) 43560–43567.
[30] C. Zhou, M. Hong, N. Hu, et al., Adv. Funct. Mater. 33 (2023) 2213310.
[31] J. Wang, F. Li, Z. Liu, et al., ACS Appl. Mater. Interfaces 13 (2021) 61205–61214.
[32] M. Yan, H. Chen, Y. Yu, et al., Adv. Energy Mater. 8 (2018) 1801066.
[33] W. Dong, D. Wang, X. Li, et al., J. Energy Chem. 48 (2020) 259–266.
[34] S. Grixti, S. Mukherjee, C.V. Singh, Energy Storage Mater. 13 (2018) 80–87.
[35] Q. Cheng, Z.X. Chen, X.Y. Li, et al., J. Energy Chem. 76 (2023) 181–186.
[36] X. Liu, H.J. Peng, B.Q. Li, et al., Angew. Chem. Int. Ed. 61 (2022) e202214037.
[37] X.Y. Li, S. Feng, C.X. Zhao, et al., J. Am. Chem. Soc. 144 (2022) 14638–14646.
[38] J.Y. Hwang, H.M. Kim, Y.K. Sun, J. Mater. Chem. A. 6 (2018) 14587–14593.
[39] C. Shi, S. Shao, C. Zong, et al., Mater. Chem. Front. 7 (2023) 145–152.
[40] J. Bai, B.J. Xi, H.Z. Mao, et al., Adv. Mater. 30 (2018) 1802310.
[41] G.H. Al-Shawesh, J. Zhu, W. Zhang, et al., Chin. Chem. Lett. 34 (2023) 108190.
[42] S.X. Sheng, J.B. Wu, X. Cong, et al., ACS Nano 13 (2019) 4133–4139.
[43] U. Lee, Y. Han, S. Lee, et al., ACS Nano 14 (2020) 919–926.
[44] K. Yang, L. Zhong, J. Qin, et al., ACS Appl. Nano Mater. 1 (2018) 3807–3816.
[45] Q. Li, Y. Zhao, H. Liu, et al., ACS Nano 13 (2019) 11921–11934.

[46] M.I. Nandasiri, L.E.C. Forero, A.M. Schwarz, et al., Chem. Mater. 29 (2017) 4728–4737.
[47] W. Sun, X. Ou, X. Yue, et al., Electrochim. Acta 207 (2016) 198–206.
[48] Y. Zhang, C. Kang, W. Zhao, et al., J. Am. Chem. Soc. 145 (2023) 1728–1739.
[49] Z. Wang, Y. Dong, H. Li, et al., Nat. Commun. 5 (2014) 5002–5009.
[50] Z.Y. Wang, L. Wang, S. Liu, G.R. Li, X.P. Gao, Adv. Funct. Mater. 29 (2019) 1901051.
[51] Y. Lu, S. Gu, J. Guo, et al., ACS Appl. Mater. Interfaces 9 (2017) 14878–14888.
[52] R. Soni, J.B. Robinson, P.R. Shearing, et al., Energy Storage Mater. 51 (2022) 97–107.
[53] Q. Gong, L. Hou, T. Li, Y. Jiao, P. Wu, ACS Nano 16 (2022) 8449–8460.
[54] Z. Deng, Z. Zhang, Y. Lai, et al., J. Electrochem. Soc. 160 (2013) A553–A558.
[55] K.C. Wasalathilake, M. Roknuzzaman, K.K. Ostrikov, G.A. Ayoko, C. Yan, RSC Adv. 8 (2018) 2271–2279.
[56] Z.W. Seh, Q. Zhang, W. Li, et al., Chem. Sci. 4 (2013) 3673–3677.
[57] J. Song, M.L. Gordin, T. Xu, et al., Angew. Chem. Int. Ed. 54 (2015) 4325–4329.
[58] S. Huang, Y.V. Lim, X. Zhang, et al., Nano Energy 51 (2018) 340–348.
[59] T. Xiao, F. Yi, M. Yang, et al., J. Mater. Chem. A 9 (2021) 16692–16698.
[60] Z. Shen, M. Cao, Z. Zhang, et al., Adv. Funct. Mater. 30 (2020) 1906661.
[61] H. Duan, K. Li, M. Xie, et al., J. Am. Chem. Soc. 143 (2021) 19446–19453.
[62] J.W. Ju, Y.T. Wang, B.B. Chen, et al., ACS Appl. Mater. Interfaces 10 (2018) 13588–13597.
[63] T. Zhang, F. Hu, W. Shao, et al., ACS Nano 15 (2021) 15027–15038.
[64] S. Zheng, Y. Wen, Y. Zhu, et al., Adv. Energy Mater. 4 (2014) 1400482.
[65] Y. Yang, C. Chen, J. Hu, et al., Chin. Chem. Lett. 29 (2018) 1777–1780.